Tunable charge to spin conversion in strontium iridate thin films

Arnoud S. Everhardt, Mahendra DC, Xiaoxi Huang, Shehrin Sayed, Tanay A. Gosavi, Yunlong Tang, Chia-Ching Lin, Sasikanth Manipatruni, Ian A. Young, Supriyo Datta, Jian-Ping Wang, and Ramamoorthy Ramesh

Phys. Rev. Materials **3**, 051201 — Published 6 May 2019

DOI: 10.1103/PhysRevMaterials.3.051201

Tunable charge to spin conversion in strontium iridate thin films

Arnoud S. Everhardt*[1,2‡], Mahendra DC*[3], Xiaoxi Huang[2], Shehrin Sayed[4,5], Tanay Gosavi[6], Yunlong Tang[1,2], Chia-Ching Lin[6], Sasikanth Manipatruni[6], Ian Young[6], Supriyo Datta[5], Jian-Ping Wang[3], Ramamoorthy Ramesh[1,2‡]

[1] Materials Sciences Division, Lawrence Berkeley National Laboratory, Berkeley, CA 94720, USA

[2] Department of Materials Science and Engineering and Department of Physics, University of California, Berkeley, CA 94720

[3] School of Physics and Astronomy, University of Minnesota, Minneapolis, MN, USA

[4] Department of Electrical Engineering and Computer Science, University of California, Berkeley, CA 94720

[5] School of Electrical and Computer Engineering, Purdue University, West Lafayette, Indiana 47907, USA

[6] Intel Corporation

* These authors contributed equally

‡ Corresponding authors: arnoudeverhardt@lbl.gov; rramesh@berkeley.edu

Abstract: Efficient charge to spin conversion is important for low power spin logic devices. Spin and charge interconversion is commonly performed using heavy metals and topological insulators, while the field of oxides is not yet fully explored. Strontium iridate thin films were grown, where the different crystal structures form a perfect playground to understand the key factors in obtaining high charge to spin conversion efficiency (i.e., large spin Hall angle). It was found that the semiconducting Sr_2IrO_4 has a spin Hall angle of ~0.1 (depending on measurement technique), which is promising for a spin-orbit coupled electronic system and comparable to Pt. In contrast, the perovskite $SrIrO_3$, reported to have a Dirac cone near the Fermi level, has a larger spin Hall angle of 0.3-0.4 degrees. The largest difference between the two materials is a large degree of spin-momentum locking in $SrIrO_3$, comparable to known topological insulators. A simple semi-classical relationship is found where the spin Hall angle increases for higher degrees of spin-momentum locking and it also increases for lower Fermi wave vectors. This relationship is then able to explain the decreased spin Hall angle below 10 nm film thickness in $SrIrO_3$, by relating it to the correspondingly higher carrier concentration (related to the higher Fermi wave vector). Breaking the commonly believed anti-correlation between resistivity and carrier concentration paves a pathway to lower power losses due to resistance while keeping large spin Hall angles.

Main text

Transition metal oxides provide a rich playground for a variety of fundamental physical phenomena that have led to discoveries such as high temperature superconductivity in cuprates, colossal magnetoresistance in doped manganites[1], and multiferroic behavior[2]. Many oxide materials are used for their versatile properties and high adaptability, ranging from metallic to insulating[3], magnetic[4,5] and, in the case of 4d and 5d transition metal oxides, large spin-orbit coupling[6]. Small variations in elemental composition[7,8], boundary conditions, interface effects[9] or strain[10] in thin films can have a profound influence on such physical phenomena. One of the scientific challenges in the field of spintronics these days is the manipulation and interconversion of spin and charge. Spintronic logic devices, such as a spin-orbit torque magnetoresistive random access memory (SOT-MRAM)[11,12], skyrmionic[13] or magnetoelectric spin orbit logic[14–16] require a low-power highly efficient interconversion of spin to charge, which is given as the spin Hall angle. There have been several studies of the (inverse) spin Hall and Rashba-Edelstein effects in heavy metals[17,18] and semiconductors[19,20]. Recently, extensions into topological insulators that exhibit large spin orbit coupling[21–25] and 2D electron gas systems[9] have revealed a larger degree of interconversion. The generally observed trend is that, for sufficiently heavy elements, increasing the resistivity leads to an enhancement of the spin and charge intercoupling[26,27], most notably in the series of increasing coupling for the heavy metals Au[28], Pt[29], Ta[18] and W[30]. A merging of spintronics with the wide tunability in electronic properties provided by oxide materials will be able to provide novel pathways towards high charge and spin coupling with lower power requirements.

Oxides, especially the ones in which one or more of the chemical sublattices is comprised of high spin-orbit coupled chemical species (e.g., Ir^{4+} in iridates) present an interesting opportunity to explore the role of strong spin-orbit coupling, tunability of electronic structure, resistivity and carrier concentrations as well as the potential to introduce correlations as an active parameter[6]. The physics in the material class of iridates[6,31–33] is driven by the electronic structure of the Ir^{4+} ion. As a direct consequence of the large atomic number, spin-orbit coupling is much stronger than the commonly used 3d elements. The competition between the increased spin-orbit coupling and the decreased electron correlation strength, *U*, due to larger orbital extension provides a rich physics playground with phenomena like topological Mott insulators, spin liquids and Weyl semimetals[6]. Several crystal classes manifest themselves within the family of iridates, particularly in the Ruddlesden-Popper series of $Sr_{n+1}Ir_nO_{3n+1}$ with its endmembers $SrIrO_3$ and Sr_2IrO_4, and in the pyrochlores with the stoichiometry $A_2Ir_2O_7$. Within each

family, an extensive range of chemical substitutions is available to systematically tune the electronic interactions.

The layered perovskite Sr_2IrO_4 manages to overcome the expected metallic state by forming several narrow bands due to strong spin-orbit interaction. Then a small, but non-zero electronic repulsion energy U (responsible for Mott insulating states) is enough to split those narrow bands to make this material weakly semiconducting with a bandgap of ~0.5 eV[34]. In contrast, the perovskite $SrIrO_3$ has an intrinsic metallic state by overcoming those band splittings due to increased dimensionality and decreased octahedral rotations[35]. However, going towards large compressive strain [31] or to lower (<5 nm) thicknesses [32], it manifests a metal-insulator transition. Furthermore, a highly interesting behavior in $SrIrO_3$, not found in Sr_2IrO_4, is its semimetallic state with a Dirac cone crossing the Fermi level, predicted theoretically[36] and found in ARPES measurements[35,37]. This indicates that the material should have a high degree of spin-momentum locking like in topological insulators and thus a large charge to spin interconversion[38].

High-quality strontium iridate thin films were grown from stoichiometric targets by Pulsed Laser Deposition of $SrIrO_3$ (Sr_2IrO_4) on an LSAT substrate[39–41] using temperature T = 700 °C (850 °C), oxygen pressure P_{O2} = 0.13 mbar (0.004 mbar), laser repetition rate = 2 Hz (1 Hz) and laser fluence = 1.5 J/cm^2 (2 J/cm^2). Ferromagnetic NiFe (permalloy, $Ni_{0.79}Fe_{0.19}$) as spin detection layer and oxide capping layers (AlO_x or MgO) were sputtered *ex-situ*. Fig. 1 shows the structure of the films with the perovskite $SrIrO_3$ and the layered structure Sr_2IrO_4. $SrIrO_3$ is on the border between metallic and insulating as expected for this strain state[39], with a minimum in the resistivity at 200 K, increased carrier concentration and decreased mobility for higher temperatures for the 10 nm thick $SrIrO_3$, while 5 nm $SrIrO_3$ has decreasing resistivity for higher temperatures combined with flat mobility and increased carrier concentration as an insulating state. So the metal-insulator transition takes place between 10 and 5 nm, higher than reported on low-strain substrates[32] due to the increased compressive strain[31] aiding in the metal-insulator transition. Sr_2IrO_4 is semiconducting over all thicknesses with >1000x higher resistivity than $SrIrO_3$. The 5 nm Sr_2IrO_4 was too resistive to measure its resistivity and the Hall coefficients could not be determined with more accuracy than a lower bound of 10^{20}-10^{21} cm^{-3}, comparable to that of metallic $SrIrO_3$.

The characterization of the charge to spin conversion was performed by looking at the effect an injected charge current in the grown spin Hall material/ferromagnet bilayer (iridate/NiFe in this study) has on the magnetization of the ferromagnet. Following an injected charge current flowing laterally along the x-

axis, the spin Hall effect generates spin currents perpendicular (along the z-axis) to the applied charge current in the iridate material as sketched in Fig 2a, while the Rashba-Edelstein effect generates non-equilibrium spin accumulation near the iridate/NiFe interface which can diffuse into the ferromagnet, also perpendicular (along the z-axis) to the charge current. Those spin currents exert a torque on the magnetization in the ferromagnetic material NiFe. The first torque exerted is the anti-damping-like torque, a torque parallel (along the y-axis) to the surface τ_{DL} or $\tau_{//}$, which produces an effective out-of-plane field H_{OOP}[42,43]. The second torque observed in these measurement configurations are the Oersted torques τ_{Oe}, which exert the torque perpendicular to the surface (along the z-axis) and they are generated by the charge current flow in the non-magnetic layer due to Ampère's law. Knowing these two torques, it becomes possible to calculate the spin Hall angle by measuring the ratio of these two torques, as both τ_{DL} and the Oersted field τ_{Oe} depend only on the current flow through the spin-orbit coupled material (iridates here), which makes it a self-consistent method independent of the individual resistivity values of the two layers. However, in some materials additionally a field-like torque is also observed, which is parallel to the Oersted field (along the z-axis) and which can be combined into a single perpendicular torque τ_L which leads to a transverse field H_T[42,43]. In this case the ratio between the two torques can no longer be used to determine spin-orbit effects. This field-like torque has been shown to be highly dependent on the spin-orbit coupled layer thickness, the ferromagnet thickness, the saturation magnetization and the relative strengths of spin Hall and Rashba effects[42,44–46], changing in magnitude and sign dependent on all these parameters.

The first technique used was spin-torque ferromagnetic resonance (ST-FMR) to determine the spin Hall angle in Sr_2IrO_4 as shown in Fig 2b. This technique passes an rf-current through a bilayer of the iridate/permalloy and the output mixing-voltage is determined as a function of the resonance frequency. This mixing voltage is analytically fitted to symmetric (*S*) and antisymmetric (*A*) components which can be converted into a spin Hall angle[47]; this has been found to be 0.06 for 5 nm of Sr_2IrO_4 and 0.11 for 10 nm of Sr_2IrO_4 (Fig 2c). The second technique is based on second-harmonic Hall measurements (SHH), which measures the transverse second harmonic voltage signal arising from a low-frequency ac-current through a Hall bar. As a reference, Fig 2d gives the first harmonic signal $R_{1\omega}$ which is the planar Hall effect. Fig 2e gives the second harmonic signal $R_{2\omega}$ which has a large $\cos(\beta)$ signal (where β is the angle between the applied current and the external field H_{ext}), which is related to H_{OOP} and a small $\cos(3\beta)$ signal, which is related to H_T. The spin Hall angle for each direction can be calculated individually from each of the components[47] by providing the resistivity of each of the layers as a

model parameter. Although the fitting of this data (Fig 2f,g) gives spin Hall angles of 0.6 for a 5 nm Sr_2IrO_4 layer and 0.4 for a 10 nm Sr_2IrO_4 layer, we elaborate below why these are likely to be inaccurate.

The field-like torque is small in this material, as concluded from the observed low *A* component for the ST-FMR and a small H_T value in SHH. The deviation between the measured spin Hall angles from the two different techniques is large (~0.1 for ST-FMR and ~0.5 for SHH). The ST-FMR spin Hall angle for Sr_2IrO_4 is similar to the 0.07 in a reference Pt material (with the same sign), using the same technique and ferromagnet layer thickness[47]. The ST-FMR should give reliable values due to the low field-like torque in this material. The SHH method gives a 0.03 spin Hall angle for the reference Pt, comparable to its ST-FMR value. However, the deviation for the SHH measurement in Sr_2IrO_4 is likely due to the large resistivity mismatch between NiFe (20 $\mu\Omega$ cm) and Sr_2IrO_4 (1 000 000 $\mu\Omega$ cm), which makes this SHH technique less accurate. Thermal effects can also play a role in this measurement. Nevertheless, the large spin Hall angle from this shows that the spin Hall angle is at least comparable to Pt, a good spin Hall material, where the promising nature of Sr_2IrO_4 comes from the strong spin-orbit electronic structure at the Fermi level.

In contrast, the sister compound $SrIrO_3$ is a metallic system on the border of a metal-insulator transition for this strain state[31,33]. The symmetric *S* component in the ST-FMR signal (Fig. 3a) looks, qualitatively, similar to the signal observed in Sr_2IrO_4 with a similar measured voltage output signal. The ST-FMR signal (Fig 3a) is not unlike Sr_2IrO_4 for the *S* component. However, the *A* component is much larger and of an opposite sign than for the Sr_2IrO_4, indicating a large field-like torque of opposite sign to the Oersted field. The spin Hall angle calculated from this type of ST-FMR measurement in $SrIrO_3$ is not able to account for this field-like torque, so only a reduced spin Hall angle of about 0.1 can be calculated from this method. SHH measurements determine τ_{DL} and $\tau_{\perp}$ and their corresponding spin Hall angles individually, which makes it more suitable for this material with a sizeable field-like torque. The first harmonic planar Hall effect $R_{1\omega}$ (Fig 3c) is similar to Sr_2IrO_4 in shape, while the second harmonic signal has additional strong contributions for $SrIrO_3$. The $\tau_{\perp}$ with its $\cos(3\beta)$ signal is large in this measurement as seen in Fig 3d. Thicker $SrIrO_3$ films (with identical NiFe ferromagnets) show an increase in H_{OOP}, and thus a stronger charge-to-spin conversion (Fig 3e), with a corresponding decrease in H_T (Fig 3f). The spin Hall angle from these two techniques is different since the SHH does not include $\tau_{\perp}$ in its calculations. The spin Hall angle for a 3 nm thin $SrIrO_3$ film is around 0.1, which is similar to that observed in Ta[46,48]. Interestingly, the spin Hall angle increases for thicker samples. Our measurements demonstrated a value as large as 0.4 on a 13 nm sample, which is comparable to that reported in W[30]

and much larger than the small, positive spin Hall angles with small field-like-torque as in Au[28] and Pt[29].

The resistivity of $SrIrO_3$ decreases for samples with higher thickness, which is opposite to the trend that the spin Hall angle increases for thicker samples. The popular belief, based on the demonstration in heavy metals[26], is that when the crystal structure does not change, samples with higher resistivity exhibit higher spin Hall angles. In addition, the lowering of the sample resistivity with increasing thickness is accompanied by a lowering of the carrier concentration. A similar trend has previously been observed in topological insulators[49,50]. As found previously (Fig 1e), a metal-insulator transition[31,33] occurs when increasing the thickness from 5 to 10 nm, and this is also the thickness regime where the resistivity and carrier concentration drastically decrease.

We relate the observed trends in spin Hall angle θ_{SH}, and carrier concentration (n_e) using the following expression

$$\theta_{SH} = \frac{J_s}{J_c} \propto \frac{2\xi p_0}{\pi} \frac{g^{\uparrow\downarrow}}{m_n} \quad (1)$$

which was derived from (i) a semiclassical model[51,52] for charge current induced spin potential in spin-orbit materials that received numerous experimental confirmation on diverse materials, in conjunction with (ii) a widely used semiclassical model (see the details of the derivation in the Supplemental Material[47]) for spin current absorption at the ferromagnet-spin-orbit metal interface[54]. Here $0 \le \xi \le 1$ is the current shunting in the ferromagnet[51], $0 \le p_0 \le 1$ is the degree of spin-momentum locking (SML) in the spin-orbit material[51,52], $g^{\uparrow\downarrow}$ is the real part of the interface spin-mixing conductance in units of m^{-2} [53], and n_m is the number of modes per unit cross-section of the SML channel which can be calculated from the Fermi wavevector k_F, of the material as $m_n = \frac{k_F^2}{2\pi}$ [54]. The Fermi wavevector k_F of the material is related to the measured carrier concentration n_e using $k_F = \sqrt[3]{3\pi^2 n_e}$. Note that the dependence on ξ, p_0, and m_n in Eq. 1 arises due to argument (i) based on which we make arguments below. The dependence on $g^{\uparrow\downarrow}$ in Eq. 1 arises due to argument (ii).

Eq. 1 suggests an increasing trend of the spin Hall angle with the decreasing electron density, which is in agreement with our experimental observations in Figs. 3(f) and 4(a), respectively. We have compared the measured spin Hall angle data with x/k_F^2 in Fig. 4(b), where x is a fitting parameter and k_F is estimated from the measured electron density. The $1/k_F^2$ dependence in Eq. 1 suggests a saturation in spin Hall angles for thicker samples since the measured electron density saturates above 10 nm. Such

saturation is in agreement with similar report[54] of spin Hall angle in $SrIrO_3$ grown on $SrTiO_3$ substrates. Using measured values of $g^{\uparrow\downarrow}$ [47] and an estimated $\xi \approx 0.1$ (rough estimation based on resistivity ratios), we roughly estimate the degree of spin-momentum locking p_0 in Sr_2IrO_4 as 0.07 and in $SrIrO_3$ as 0.2-0.6. The estimated large value of p_0 in $SrIrO_3$ is comparable to that typically seen for topological insulators[55–61], however, careful spin-potentiometric measurements need to be done for confirmation of the estimated p_0 which we leave as future work.

The observation that both resistivity and electron density are decreasing for thicker samples imply a larger electron mean free path λ, for thicker samples. We estimate[53] the mean free path using[47]:

$$\lambda = h/(q^2 \rho m_n). \quad (2)$$

The estimated mean free path is ~60 pm for 3 nm thick sample which increases and saturates to ~1 nm for samples thicker than 8 nm, as shown in Fig 4b.

So, while in heavy metals it is commonly assumed that an increase in resistivity gives larger spin Hall angles, the thickness dependent spin Hall angle measurements in $SrIrO_3$ show that this relationship does not hold, but rather it is the carrier concentration that determines the efficiency. While in most materials the carrier concentration and resistivity are anti-correlated, here this correlation is broken, like in topological insulators. As already shown by previous work, the Weyl semimetal nature of $SrIrO_3$ suggests the existence of band-crossing effects. Such a topological nature further manifests itself in the large degree of spin-momentum locking p_0 of 0.2-0.6, due to the Dirac cone like nature at the Fermi surface in $SrIrO_3$, producing a large spin Hall angle of 0.3-0.5 and a large degree of field-like torque. In contrast, as expected from prior studies, Sr_2IrO_4, which does not have a topological nature to its electronic structure exhibits a reduced spin Hall angle of ~0.1 (comparable to Pt) and small field-like-torque while still being promising with its spin-orbit dominated electronic structure. Finally, the large tunability of electronic structure through crystal chemistry and epitaxial constraint in these oxides make it possible to further explore relationships and patterns in the search of larger spin Hall angles for efficient charge and spin interconversion for low power spin logic devices.

Figures

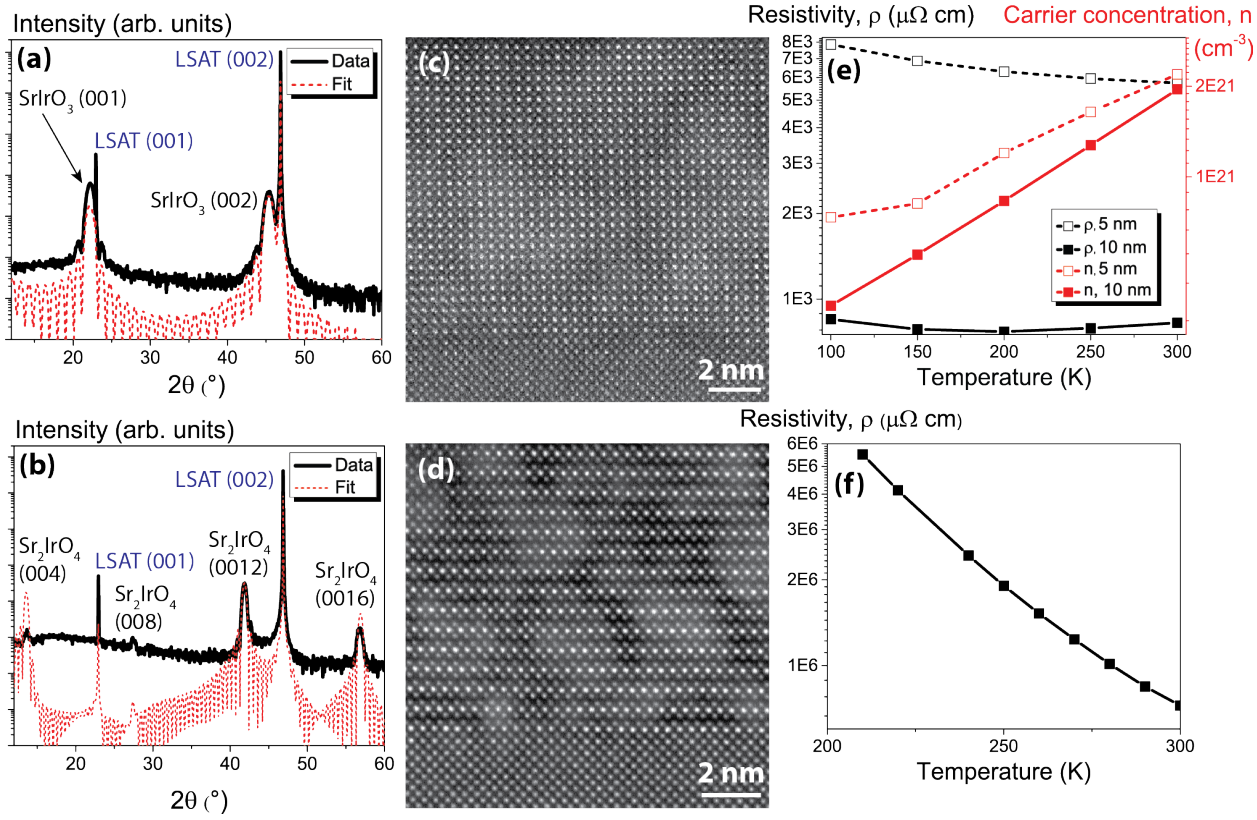

FIG. 1. (a,b) X-Ray Diffraction scan of $SrIrO_3$ and Sr_2IrO_4, along with a diffraction pattern calculated from their simulated crystal structures. The agreement between the theoretical fits and the data shows that the right crystal structures have been formed. Lattice parameters are determined from the Bragg peak (00l) indices to be LSAT (substrate) = 3.87 Å, $SrIrO_3$ = 3.98 Å, and Sr_2IrO_4 = 25.8 Å. (c,d) Transmission Electron Microscopy images of $SrIrO_3$ and Sr_2IrO_4, showing the perovskite and layered structures, respectively, of the two materials. A NiFe/AlO_x top layer is grown on the $SrIrO_3$. (e) Resistivity ρ, and electron carrier concentration n, mobility of 5 and 10 nm thick films of $SrIrO_3$. (f) Resistivity ρ, data for 10 nm of Sr_2IrO_4.

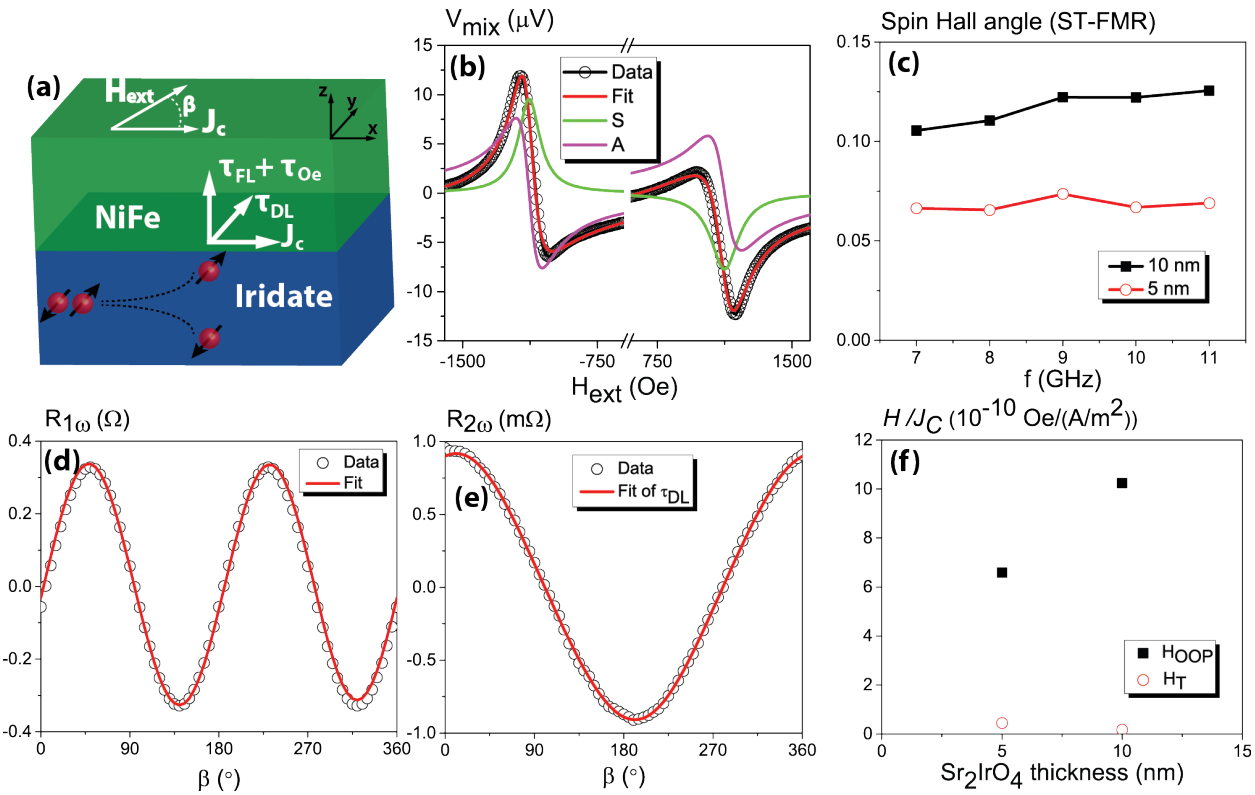

FIG. 2. (a) The different types of torques present in a ferromagnet/iridate bilayer of materials. A charge current J_c, driven through the bilayer, couples to the magnetization M in the ferromagnet in three ways. The anti-damping-like torque τ_{DL} acts parallel to the surface and couples to out-of-plane magnetization. The field-like torque τ_{FL} acts perpendicular to the surface and couples to transverse magnetization, while the Oersted torque τ_{Oe} acts along the same axis as the field-like torque (combined in $\tau_{\perp}$). The external magnetic field (H_{ext}) can be applied under an in-plane angle β with respect to the current direction. (b) ST-FMR resonance line shape for Sr_2IrO_4 (10 nm)/NiFe (6 nm) bilayer structure under 5 mA and a frequency of 9 GHz oscillating rf current. Lorentzian trial functions extracted symmetric and antisymmetric components from the mixing voltage V_{mix} (the obtained quantity from the measurement), represented by the black and green solid lines, respectively. (c) Spin Hall angles extracted from the ST-FMR method for different frequencies f, in 5 and 10 nm of Sr_2IrO_4. (d) First harmonic $R_{1\omega}$ and (e) Second Harmonic $R_{2\omega}$ signals of the SHH measurement in a Sr_2IrO_4 (10 nm)/NiFe (6 nm) bilayer structure under a driving field of 10 mA at 5000 Oe. $R_{1\omega}$ gives the planar Hall effect, while $R_{2\omega}$ gives a combination of different angular contributions, which can be separated into the different contributions. Here only a cos(β) contribution is measured, which gives a τ_{DL}. (f) H_{OOP} and (g) H_T fields as a function of applied current, from which the spin Hall angle is calculated.

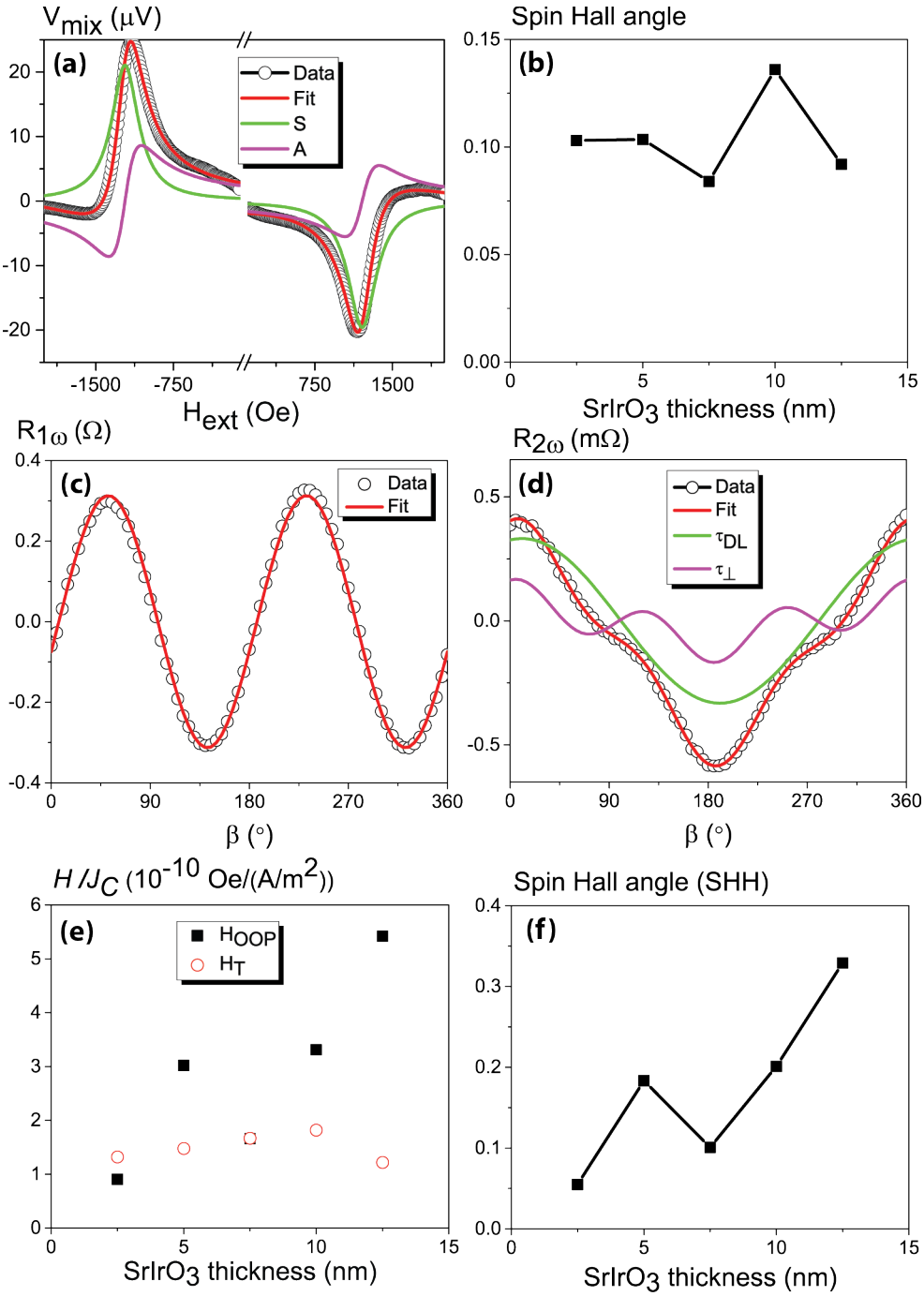

FIG. 3. (a) ST-FMR in $SrIrO_3$ (5 nm)/NiFe (6 nm) under an rf current of 10 mA and a frequency of 9 GHz. (b) Spin Hall angle calculated from ST-FMR. (c) $R_{1\omega}$ and (d) $R_{2\omega}$ signals of the SHH measurement in a Sr_2IrO_4 (10 nm)/NiFe (6 nm) bilayer structure under a driving field of 10 mA at 5000 Oe magnetic field, separated into their components τ_{DL} by $\cos(\beta)$ and $\tau_{\perp}$ by $\cos(3\beta)$. (e) H_{OOP} and (f) H_T fields as a function of applied current. (g) Spin Hall angle calculated from SHH measurement from the H_{OOP}.

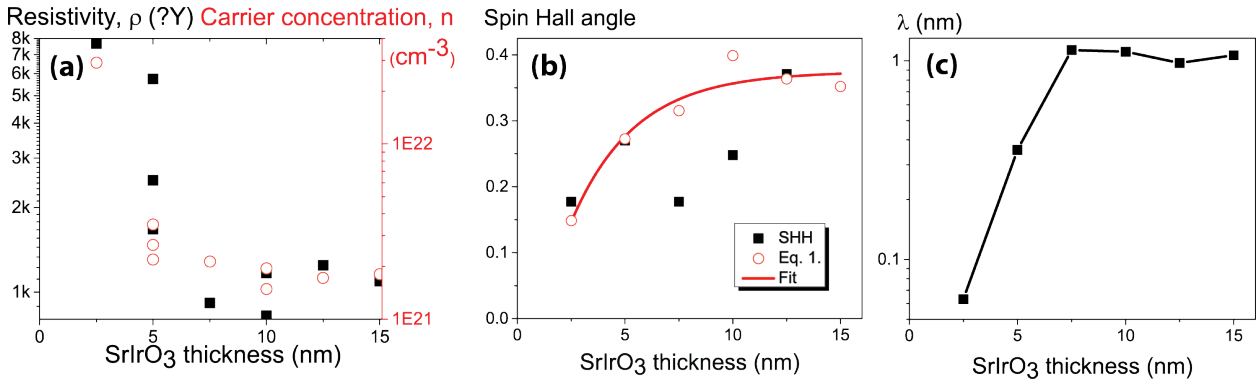

FIG. 4. (a) Resistivity and carrier concentration calculated from Hall measurements of $SrIrO_3$ films of different thickness without capping layer. (b) Calculated spin Hall angles with a fixed fitted *x* factor of 5 (10^{18} m^{-2}) from Eq. 1 with an exponential fit, given together with the measured spin Hall angles. (c) Electron mean free path λ as determined from Eq. 2 with the same fixed *x* factor as in (b).

Acknowledgements

A.S.E., Y.T. and R.R. acknowledge support from the U.S. Department of Energy, Office of Science, Basic Energy Sciences, Materials Sciences and Engineering Division under Contract No. DE-AC02-05-CH11231 within the Quantum Materials program (KC2202). Portions of the devices were fabricated in the UC Berkeley Marvell Nanofabrication Laboratory. M.DC., X.H., J.-P.W. and R.R. were supported in part by ASCENT, one of six centers in JUMP, a Semiconductor Research Corporation (SRC) program sponsored by DARPA. Portions of this work were conducted in the Minnesota Nano Center, which is supported by the National Science Foundation through the National Nano Coordinated Infrastructure Network (NNCI) under Award Number ECCS-1542202.

References

[1] E. Dagotto. Nanoscale Phase Separation and Colossal Magnetoresistance. (Springer-Verlag Berlin Heidelberg, 2003).

[2] N. A. Spaldin and R. Ramesh. Progress in multiferroics and magnetoelectrics (unpublished). Nat. Mater. (2019).

[3] S. Catalano, M. Gibert, J. Fowlie, J. Íñiguez, J.-M. Triscone, and J. Kreisel. Rare-earth nickelates $RNiO_3$: thin films and heterostructures. Reports Prog. Phys. **81,** 046501 (2018).

[4] J. Wang, J. B. Neaton, H. Zheng, V. Nagarajan, S. B. Ogale, B. Liu, D. Viehland, V. Vaithyanathan, D. G. Schlom, U. V. Waghmare, *et al*. Epitaxial $BiFeO_3$ multiferroic thin film heterostructures. Science **299,** 1719–1722 (2003).

[5] N. Vlietstra, J. Shan, V. Castel, B. J. Van Wees, and J. Ben Youssef. Spin-Hall magnetoresistance in platinum on yttrium iron garnet: Dependence on platinum thickness and in-plane/out-of-plane magnetization. Phys. Rev. B **87,** 184421 (2013).

[6] W. Witczak-Krempa, G. Chen, Y. B. Kim, and L. Balents. Correlated Quantum Phenomena in the Strong Spin-Orbit Regime. Annu. Rev. Condens. Matter Phys. **5,** 57–82 (2014).

[7] Z. Cheng, X. Wang, S. Dou, H. Kimura, and K. Ozawa. Improved ferroelectric properties in multiferroic $BiFeO_3$ thin films through La and Nb codoping. Phys. Rev. B **77,** 092101 (2008).

[8] S. Majumdar and S. Van Dijken. Pulsed laser deposition of $La_{1-x}Sr_xMnO_3$: Thin-film properties and spintronic applications. J. Phys. D. Appl. Phys. **47,** 034010 (2014).

[9] E. Lesne, Y. Fu, S. Oyarzun, J. C. Rojas-Sánchez, D. C. Vaz, H. Naganuma, G. Sicoli, J.-P. Attané, M. Jamet, E. Jacquet, *et al.* Highly efficient and tunable spin-to-charge conversion through Rashba coupling at oxide interfaces. Nat. Mater. **15,** 1261–1266 (2016).

[10] J. H. Haeni, P. Irvin, W. Chang, R. Uecker, P. Reiche, Y. L. Li, S. Choudhury, W. Tian, M. E. Hawley, B. Craigo, *et al.* Room-temperature ferroelectricity in strained $SrTiO_3$. Nature **430,** 758–761 (2004).

[11] N. Sato, F. Xue, R. M. White, C. Bi, and S. X. Wang. Two-terminal spin–orbit torque magnetoresistive random access memory. Nat. Electron. **1,** 508–511 (2018).

[12] M. Cubukcu, O. Boulle, M. Drouard, K. Garello, C. Onur Avci, I. M. Miron, J. Langer, B. Ocker, P. Gambardella, and G. Gaudin. Spin-orbit torque magnetization switching of a three-terminal perpendicular magnetic tunnel junction. Appl. Phys. Lett. **104,** 042406 (2014).

[13] M. G. Mankalale, Z. Zhao, J.-P. Wang, and S. S. Sapatnekar. SkyLogic – A proposal for a skyrmion logic device. arXiv 1811.02016

[14] S. Manipatruni, D. E. Nikonov, C.-C. Lin, T. A. Gosavi, H. Liu, B. Prasad, Y.-L. Huang, E. Bonturim, R. Ramesh, and I. A. Young. Scalable energy-efficient magnetoelectric spin–orbit logic. Nature **565,** 35–42 (2018).

[15] S. Manipatruni, D. E. Nikonov, and I. A. Young. Beyond CMOS computing with spin and polarization. Nat. Phys. **14,** 338–343 (2018).

[16] M. G. Mankalale, Z. Liang, Z. Zhao, C. H. Kim, J.-P. Wang, and S. S. Sapatnekar. CoMET : Composite-Input Magnetoelectric-. IEEE J. Explor. Solid-State Comput. Devices Circuits **3,** 27–36 (2017).

[17] S. O. Valenzuela and M. Tinkham. Direct electronic measurement of the spin Hall effect. Nature **442,** 176–179 (2006).

[18] L. Liu, C.-F. Pai, Y. Li, H. W. Tseng, D. C. Ralph, and R. A. Buhrman. Spin-Torque Switching with the Giant Spin Hall Effect of Tantalum. Science **336,** 555–558 (2012).

[19] Y. K. Kato, R. C. Myers, A. C. Gossard, and D. D. Awschalom. Observation of the Spin Hall. Science **306,** 1910–1913 (2004).

[20] K. Ando and E. Saitoh. Observation of the inverse spin Hall effect in silicon. Nat. Commun. **2,** 626–629 (2012).

[21] M. DC, R. Grassi, J. Y. Chen, M. Jamali, D. Reifsnyder Hickey, D. Zhang, Z. Zhao, H. Li, P. Quarterman, Y. Lv, *et al.* Room-temperature high spin–orbit torque due to quantum confinement in sputtered $Bi_xSe_{(1-x)}$ films. Nat. Mater. **17,** 800–807 (2018).

[22] J. C. R. Sánchez, L. Vila, G. Desfonds, S. Gambarelli, J. P. Attané, J. M. De Teresa, C. Magén, and A. Fert. Spin-to-charge conversion using Rashba coupling at the interface between non-magnetic materials. Nat. Commun. **4,** 2944 (2013).

[23] A. R. Mellnik, J. S. Lee, A. Richardella, J. L. Grab, P. J. Mintun, M. H. Fischer, A.Vaezi, A. Manchon,

E.-A. Kim, N. Samarth, *et al.* Spin-transfer torque generated by a topological insulator. Nature **511,** 449–451 (2014).

[24] Y. Wang, P. Deorani, K. Banerjee, N. Koirala, M. Brahlek, S. Oh, and H. Yang. Topological surface states originated spin-orbit torques in Bi_2Se_3. Phys. Rev. Lett. **114,** 257202 (2015).

[25] M. Jamali, J. S. Lee, J. S. Jeong, F. Mahfouzi, Y. Lv, Z. Zhao, B. K. Nikolic, K. A. Mkhoyan, N. Samarth, and J.-P. Wang. Giant Spin Pumping and Inverse Spin Hall Effect in the Presence of Surface and Bulk Spin-Orbit Coupling of Topological Insulator Bi_2Se_3. Nano Lett. **15,** 7126–7132 (2015).

[26] E. Sagasta, Y. Omori, S. Vélez, R. Llopis, C. Tollan, A. Chuvilin, L. E. Hueso, M. Gradhand, Y.C. Otani, and F. Casanova. Unveiling the mechanisms of the spin Hall effect in Ta. Phys. Rev. B **98,** 060410(R) (2018).

[27] T. Tanaka, H. Kontani, M. Naito, T. Naito, D. S. Hirashima, K. Yamada, and J. Inoue. Intrinsic spin Hall effect and orbital Hall effect in 4d and 5d transition metals. Phys. Rev. B **77,** 165117 (2008).

[28] O. Mosendz, V. Vlaminck, J. E. Pearson, F. Y. Fradin, G. E. W. Bauer, S. D. Bader, and A. Hoffmann. Detection and quantification of inverse spin Hall effect from spin pumping in permalloy/normal metal bilayers. Phys. Rev. B **82,** 214403 (2010).

[29] T. Kimura, Y. Otani, T. Sato, S. Takahashi, and S. Maekawa. Room-temperature reversible spin hall effect. Phys. Rev. Lett. **98,** 156601 (2007).

[30] C. F. Pai, L. Liu, Y. Li, H. W. Tseng, D. C. Ralph, and R. A. Buhrman. Spin transfer torque devices utilizing the giant spin Hall effect of tungsten. Appl. Phys. Lett. **101,** 122404 (2012).

[31] L. Zhang, Q. Liang, Y. Xiong, B. Zhang, L. Gao, H. Li, Y. B. Chen, J. Zhou, S.-T. Zhang, Z.-B. Gu, *et al.* Tunable semimetallic state in compressive-strained $SrIrO_3$ films revealed by transport behavior. Phys. Rev. B **91,** 035110 (2015).

[32] A. Biswas, K. S. Kim, and Y. H. Jeong. Metal insulator transitions in perovskite $SrIrO_3$ thin films. J. Appl. Phys. **116**, 213704 (2014).

[33] L. Hao, D. Meyers, M. P. M. Dean, and J. Liu. Novel spin-orbit coupling driven emergent states in iridate-based heterostructures. J. Phys. Chem. Solids 1–15 (2017).

[34] B. J. Kim, H. Jin, S. J. Moon, J.-Y. Kim, B.-G. Park, C. S. Leem, J. Yu, T. W. Noh, C. Kim, S.-J. Oh, *et al.*

Novel Jeff = 1/2 Mott State Induced by Relativistic Spin-Orbit Coupling in Sr2IrO4. Phys. Rev. Lett. **101,** 076402 (2008).

[35] Y. F. Nie, P. D. C. King, C. H. Kim, M. Uchida, H. I. Wei, B. D. Faeth, J. P. Ruf, J. P. C. Ruff, L. Xie, X. Pan, *et al.* Interplay of Spin-Orbit Interactions, Dimensionality, and Octahedral Rotations in Semimetallic SrIrO3. Phys. Rev. Lett. **114,** 016401 (2015).

[36] J. M. Carter, V. V. Shankar, M. A. Zeb, and H. Y. Kee. Semimetal and topological insulator in perovskite iridates. Phys. Rev. B **85,** 115105 (2012).

[37] Z. T. Liu, M. Y. Li, Q. F. Li, J. S. Liu, W. Li, H. F. Yang, Q. Yao, C. C. Fan, X. G. Wan, Z. Wang, *et al.* Direct observation of the Dirac nodes lifting in semimetallic perovskite SrIrO3 thin films. Sci. Rep. **6,** 30309 (2016).

[38] A. S. Patri, K. Hwang, H. Lee, and Y. B. Kim. Theory of Large Intrinsic Spin Hall Effect in Iridate Semimetals. Sci. Rep. **8,** 8052 (2018).

[39] J. H. Gruenewald, J. Nichols, J. Terzic, G. Cao, J. W. Brill, and S. S. A. Seo. Compressive strain-induced metal-insulator transition in orthorhombic $SrIrO_3$ thin films. J. Mater. Res. **29,** 2491–2496 (2014).

[40] C. Rayan Serrao, J. Liu, J. T. Heron, G. Singh-Bhalla, A. Yadav, S. J. Suresha, R. J. Paull, D. Yi, J.-H. Chu, M. Trassin, *et al.* Epitaxy-distorted spin-orbit Mott insulator in Sr_2IrO_4 thin films. Phys. Rev. B **87,** 085121 (2013).

[41] J. Nichols, J. Terzic, E. G. Bittle, O. B. Korneta, L. E. De Long, J. W. Brill, G. Cao, and S. S. A. Seo. Tuning electronic structure via epitaxial strain in Sr_2IrO_4 thin films. Appl. Phys. Lett. **102,** 141908 (2013).

[42] Y. Ou, C. F. Pai, S. Shi, D. C. Ralph, and R. A. Buhrman. Origin of fieldlike spin-orbit torques in heavy metal/ferromagnet/oxide thin film heterostructures. Phys. Rev. B **94,** 140414(R) (2016).

[43] T. D. Skinner, M. Wang, A. T. Hindmarch, A. W. Rushforth, A. C. Irvine, D. Heiss, H. Kurebayashi, and A. J. Ferguson. Spin-orbit torque opposing the Oersted torque in ultrathin Co/Pt bilayers. Appl. Phys. Lett. **104,** 062401 (2014).

[44] R. Ramaswamy, X. Qiu, T. Dutta, S. D. Pollard, and H. Yang. Hf thickness dependence of spin-orbit torques in Hf/CoFeB/MgO heterostructures. Appl. Phys. Lett. **108,** 202406 (2016).

[45] J. Kim, J. Sinha, M. Hayashi, M. Yamanouchi, S. Fukami, T. Suzuki, S. Mitani, and H. Ohno. Layer thickness dependence of the current-induced effective field vector in Ta|CoFeB|MgO. Nat. Mater. **12,** 240–245 (2013).

[46] G. Allen, S. Manipatruni, D. E. Nikonov, M. Doczy, and I. A. Young. Experimental demonstration of the coexistence of spin Hall and Rashba effects in β-tantalum/ferromagnet bilayers. Phys. Rev. B **91,** 144412 (2015).

[47] See Supplemental Material at [URL will be inserted by publisher] for the details on the measurement technique and the extraction of the spin Hall angles from the ST-FMR and SHH techniques and the derivation of the spin Hall angle and mean free path equations.

[48] L. Liu, T. Moriyama, D. C. Ralph, and R. A. Buhrman. Spin-torque ferromagnetic resonance induced by the spin Hall effect. Phys. Rev. Lett. **106,** 036601 (2011).

[49] Y. S. Kim, M. Brahlek, N. Bansal, E. Edrey, G. A. Kapilevich, K. Iida, M. Tanimura, Y. Horibe, S.-W. Cheong, and S. Oh. Thickness-dependent bulk properties and weak antilocalization effect in topological insulator Bi_2Se_3. Phys. Rev. B **84,** 073109 (2011).

[50] J. Suh, K. M. Yu, D. Fu, X. Liu, F. Yang, J. Fan, D. J. Smith, Y.-H. Zhang, J. K. Furdyna, C. Dames, *et al.* Simultaneous Enhancement of Electrical Conductivity and Thermopower of Bi_2Te_3 by Multifunctionality of Native Defects. Adv. Mater. **27,** 3681–3686 (2015).

[51] S. Sayed, S. Hong, and S. Datta. Multi-Terminal Spin Valve on Channels with Spin-Momentum Locking. Sci. Rep. **6,** 35658 (2016).

[52] S. Sayed, S. Hong, and S. Datta. Transmission Line Model for Materials with Spin-Momentum Locking. Phys. Rev. Appl. **10,** 054044 (2018).

[53] Y. T. Chen, S. Takahashi, H. Nakayama, M. Althammer, S. T. B. Goennenwein, E. Saitoh, and G. E. W. Bauer. Theory of spin Hall magnetoresistance (SMR) and related phenomena. Phys. Rev. B **87,** 144411 (2013).

[54] T. Nan, T. J. Anderson, J. Gibbons, K. Hwang, N. Campbell, H. Zhou, Y. Q. Dong, and G. Y. Kim. Anisotropic spin-orbit torque generation in epitaxial $SrIrO_3$ by symmetry design. arXiv 1808.06650 (2018).

[55] J. Tang, L.-T. Chang, X. Kou, K. Murata, E. S. Choi, M. Lang, Y. Fan, Y. Jiang, M. Montazeri, W.

Jiang, *et al.* Electrical Detection of Spin-Polarized Surface States Conduction in $(Bi_{0.53}Sb_{0.47})_2Te_3$ Topological Insulator. Nano Lett. **14,** 5423–5429 (2014).

[56] L. Liu, A. Richardella, I. Garate, Y. Zhu, N. Samarth, and C. T. Chen. Spin-polarized tunneling study of spin-momentum locking in topological insulators. Phys. Rev. B **91,** 235437 (2015).

[57] F. Yang, S. Ghatak, A. A. Taskin, K. Segawa, Y. Ando, M. Shiraishi, Y. Kanai, K. Matsumoto, A. Rosch, and Y. Ando. Switching of charge-current-induced spin polarization in the topological insulator $BiSbTeSe_2$. Phys. Rev. B **94,** 075304 (2016).

[58] C. H. Li, O. M. J. Van't Erve, J. T. Robinson, Y. Liu, L. Li, and B. T. Jonker. Electrical detection of charge-current-induced spin polarization due to spin-momentum locking in Bi_2Se_3. Nat. Nanotechnol. **9,** 218–224 (2014).

[59] J. S. Lee, A. Richardella, D. R. Hickey, K. A. Mkhoyan, and N. Samarth. Mapping the chemical potential dependence of current-induced spin polarization in a topological insulator. Phys. Rev. B **92,** 155312 (2015).

[60] J. Tian, I. Miotkowski, S. Hong, and Y. P. Chen. Electrical injection and detection of spin-polarized currents in topological insulator Bi_2Te_2Se. Sci. Rep. **5,** 14293 (2015).

[61] A. Dankert, J. Geurs, M. V. Kamalakar, S. Charpentier, and S. P. Dash. Room temperature electrical detection of spin polarized currents in topological insulators. Nano Lett. **15,** 7976–7981 (2015).